Journal of Alloys and Compounds 501 (2010) 30–36

Contents lists available at ScienceDirect

Journal of Alloys and Compounds

journal homepage: www.elsevier.com/locate/jallcom

Review

Structural and magnetic properties of $(La_{0.70-x}Y_x)Ba_{0.30}Mn_{1-x}Fe_xO_3$ perovskites simultaneously doped on A and B sites ($0.0 \leq x \leq 0.30$)

Nabil Kallel[a,*], Sonia Ben Abdelkhalek[a], Sami Kallel[a], Octavio Peña[b], Mohamed Oumezzine[a]

[a] Laboratoire de Physico-chimie des Matériaux, Département de Physique, Faculté des Sciences de Monastir, BP 22, 5019 Monastir, Tunisia
[b] Sciences Chimiques de Rennes, UMR 6226-CNRS, Université de Rennes 1, 35042 Rennes Cedex, France

ARTICLE INFO

Article history:
Received 28 February 2010
Received in revised form 4 April 2010
Accepted 10 April 2010
Available online 21 April 2010

Keywords:
Perovskites
Double-exchange
Super-exchange
A-site and B-site substitution
Rietveld analysis
Spin-glass behavior

ABSTRACT

We present the structural and magnetic properties of polycrystalline samples of the solid solution $(La_{0.70-x}Y_x)Ba_{0.30}Mn_{1-x}Fe_xO_3$ ($x = 0.00$, 0.10, 0.20 and 0.30). Samples have been prepared by a conventional solid-state reaction method in air. Rietveld refinements of the X-ray powder diffraction data show a structural transition from rhombohedral ($R\bar{3}c$) to orthorhombic ($Pbnm$) symmetry when $x \geq 0.10$. The ZFC, FC and $M(H)$ measurements lead to conclude that the samples with $x \geq 0.10$ behave like spin-glass systems. The substitution of Mn^{3+} ions by Fe^{3+} ions triggers antiferromagnetic interactions between the Fe^{3+} and Mn^{4+} spins. The values of the magnetization ($M(H)$) decrease when increasing the Fe content. On the basis of a simple model of Mn and Fe spins pointing in opposite directions, we found the experimental data close to the calculated values, confirming the antiferromagnetic alignment between Fe and Mn moments.

Contents

1. Introduction

Perovskite type $Ln_{1-x}A_xMnO_3$ phases (Ln = trivalent lanthanide, A = Ca^{2+}, Sr^{2+}, Ba^{2+}) exhibit giant magnetoresistances (GMR) [1,2]. The transport and magnetic properties of the substituted manganites depend on their structure, composition, and the oxidation states of Mn. The substitution at the La site by a divalent metal ion like Ca, Ba or Sr induces ferromagnetism in the antiferromagnetic insulator $LaMnO_3$ sample because of the changes in the oxidation state of Mn from Mn^{3+} to Mn^{4+}. This shows that the substitution at the A-site does ultimately affect the Mn-site ion in the $Ln_{1-x}A_xMnO_3$ perovskite structure. This gives rise to double-exchange [3], a transfer of spin-polarised electrons from Mn^{3+} to Mn^{4+}, below the Curie temperature.

The introduction of a transition metal ion M^{3+} into the manganese site of $La_{0.7}Ba_{0.3}MnO_3$ manganites can destroy the long-range ferromagnetic order and shift the magnetic and electric ordering temperatures toward lower values [4]. Depending on the size mismatch of A-site or B-site ions in the ABO_3-type perovskites, the Mn^{3+}–O^{2-}–Mn^{4+} network can be changed. In this way, one can modulate the competition between the double-exchange, super-exchange and Coulomb interactions among the Mn ions. Compared to the A-site doping, B-site doping will not only modify the crucial Mn^{3+}–O^{2-}–Mn^{4+} network but also brings about new interactions

* Corresponding author. Tel.: +216 97 600 841; fax: +216 73 500 278.
E-mail addresses: kallel_nabil@yahoo.fr, Nabil.Kallel@fsm.rnu.tn (N. Kallel).

0925-8388/$ – see front matter © 2010 Elsevier B.V. All rights reserved.
doi:10.1016/j.jallcom.2010.04.073

between the center Mn ions and the dopants. Doping by magnetic ions such as Fe^{3+} at Mn-site causes additional magnetic coupling. Until now, only scarce studies have been carried out concerning simultaneous doping of A-site and B-site of ABO_3-type perovskites. In this context, our goal is to study the influence of the simultaneous substitution of Y^{3+} ion at the A-site and of Fe^{3+} magnetic ion at the Mn-site on the structural as well as magnetic properties of $La_{0.7}Ba_{0.3}MnO_3$.

2. Experimental details

Polycrystalline samples $(La_{0.70-x}Y_x)Ba_{0.30}Mn_{1-x}Fe_xO_3$ with $0 \le x \le 0.30$ were prepared by a conventional solid-state reaction method in air. The starting reagents, La_2O_3, Y_2O_3, $BaCO_3$, MnO_2 and Fe_2O_3 (dried before use at 400 K in order to remove any absorbed water) were weighted in stoichiometric proportions. The mixed powders were first heated in air at 1173 K during 72 h to achieve decarbonation. After grinding, they were heated again at 1473 K for 24 h in air to ensure homogenization. Intermediate cooling and mechanical grinding steps were repeated in order to get an accurate homogenization and complete reaction. The powders were pressed into pellet forms under 4 T/cm^2 and sintered at 1673 K for 2 days in air with several periods of grinding and repelleting. Finally, these pellets were quenched to room temperature. This step was carried out in order to keep the structure at the annealing temperature.

The X-ray powder diffraction patterns were recorded with a Bruker AXS D8 ADVANCE diffractometer with Cu radiation and $20^\circ \le 2\theta \le 120^\circ$ with steps of 0.02° and counting time of 16 s per step. The structure refinement was carried out by Rietveld analysis [5] of the X-ray powder diffraction data using the FullProf software (version March 2005-LLB-LCSIM). The microstructure was examined in a scanning electron microscope (SEM) at room temperature on a JSM-6400 apparatus working at 20 kV. Chemical composition was determined using energy dispersive X-ray analysis (EDX). Magnetic properties were explored with an MPMS-XL5 Quantum Design SQUID magnetometer ($2 \le T \le 400$ K) at fields between 0 and 5 T. In the zero-field-cooled (ZFC) measurement the sample was cooled down from room temperature to 2 K before a magnetic field was applied, subsequently heating the sample while recording. In the field-cooled (FC) measurement the sample was cooled in an applied field from room temperature to 2 K.

3. Results and discussion

3.1. Energy dispersive analysis

In order to check the existence of all elements in the $(La_{0.70-x}Y_x)Ba_{0.30}Mn_{1-x}Fe_xO_3$ ($x = 0$, 0.10, 0.20 and 0.30) compounds, energy dispersive X-ray analysis was performed. The EDX spectra (not presented here) reveals the presence of La, Y, Ba, Mn, Fe and O, which confirms that there is no loss of any integrated element during sintering. The typical cationic composition for the $(La_{0.70-x}Y_x)Ba_{0.30}Mn_{1-x}Fe_xO_3$ samples evaluated from EDX analysis is presented in Table 1. The EDX analysis shows that the chemical compositions of these compounds are close to the nominal ones (La:Y:Ba:Mn:Fe = $(0.70-x)$:x:0.30:$(1-x)$:x) within the limits of accuracy of the technique ($x \pm 0.01$).

3.2. SEM observations and microstructure

Fig. 1a shows the SEM photographs for the $(La_{0.70-x}Y_x)Ba_{0.30}Mn_{1-x}Fe_xO_3$ samples sintered at 1673 K for $x = 0.0$, 0.10, 0.20 and 0.30. The SEM photographs represent a strongly connected grains. These photographs show a small decrease of the grain size when the content of Y^{3+} and Fe^{3+} increases. This is also clear from the particle size calculation done by using Debye–Scherrer (D–Sc) formula [6].

Table 1
Results of EDX analysis.

	Typical cationic composition from EDX					Nominal composition
	La	Y	Ba	Mn	Fe	
$x = 0$	0.78	–	0.29	0.93	–	$La_{0.7}Ba_{0.3}MnO_3$
$x = 0.10$	0.65	0.09	0.30	0.86	0.10	$La_{0.6}Y_{0.1}Ba_{0.3}Mn_{0.9}Fe_{0.1}O_3$
$x = 0.20$	0.51	0.18	0.31	0.78	0.22	$La_{0.5}Y_{0.2}Ba_{0.3}Mn_{0.8}Fe_{0.2}O_3$
$x = 0.30$	0.41	0.28	0.31	0.68	0.32	$La_{0.4}Y_{0.3}Ba_{0.3}Mn_{0.7}Fe_{0.3}O_3$

Table 2
Variation of the particle size with x in $(La_{0.70-x}Y_x)Ba_{0.30}Mn_{1-x}Fe_xO_3$ samples.

Sample	D_{D-Sc}
$x = 0$	~1.23 nm
$x = 0.10$	~1.20 nm
$x = 0.20$	~1.10 nm
$x = 0.30$	~0.50 nm

The average grain size (D_{D-Sc}) from X-ray diffraction (XRD) peaks can be calculated by $D_{D-Sc} = 0.9\lambda/\beta\cos\theta$, where λ is the X-ray wavelength employed, θ is the diffraction angle of the most intense peak and β is the experimental full-width at half-maximum (FWHM). Values obtained for D_{D-Sc} are given in Table 2.

For $x = 0.20$ and 0.30, the micrographs obtained with backscattered electrons (BSE scanning mode) show different contrast zones (Fig. 1b). This remark may suggest the presence of impurities or the presence of two phases. These points will be confirmed by the Rietveld analyses of X-ray diffraction data, as discussed latter.

3.3. Structural analysis

The phase purity and lattice parameters of the synthesized samples were examined by means of powder X-ray diffraction at room temperature. The crystal structure for $La_{0.70}Ba_{0.30}MnO_3$ sample was refined on the basis of the $R\bar{3}c$ symmetry in the hexagonal system. Previous works show an hexagonal structure for the same compound $La_{0.70}Ba_{0.30}MnO_3$ [7,8]. No traces of secondary phases were detected for this sample. The sample with $x = 0.10$, 0.20 and 0.30 becomes orthorhombic (*Pbnm*). There are some peaks that do not refine in *Pbnm*-orthorhombic structure for the sample with $x = 0.20$ and 0.30. These peaks were identified with X'Pert HighScore Plus software (with PDF2003 data) and related to the presence of a minor $YMnO_3$ phase, which was refined as a secondary phase.

Fig. 2 shows Rietveld refinement patterns of $(La_{0.50}Y_{0.20})Ba_{0.30}Mn_{0.80}Fe_{0.20}O_3$ and $(La_{0.40}Y_{0.30})Ba_{0.30}Mn_{0.70}Fe_{0.30}O_3$. The structural parameters obtained by Rietveld refinements of the X-ray powder diffraction data are listed in Table 3. Results for the $YMnO_3$ phase are given in Table 4. Early works in the 1960s established $YMnO_3$ to be ferroelectric with space group $P6_3cm$ [9,10]. The structural transition from rhombohedral to orthorhombic can be explained by the insertion of Y^{3+} (1.06 Å) having a very small ionic radius compared to La^{3+} (1.216 Å). Indeed the variation of the mean ionic radius of A-site leads to the distortion of MnO_6 octahedra and related to the tolerance factor. Nevertheless, the substitution of Mn^{3+} (0.65 Å) by Fe^{3+} (0.645 Å) does not cause additional distortion since the mean ionic radius of the B-site decreases very slightly according to x. It provokes just a little influence on the tolerance factor. Previous work shows that $(La_{0.7}Ca_{0.3})Mn_{1-x}Fe_xO_3$ samples with $0 \le x \le 0.12$ crystallize in an orthorhombic structure (*Pbnm*) [11]. The lattice parameters are essentially independent of the Fe rate.

Table 4 shows that the weight fractions of the secondary phase $YMnO_3$ do not exceed 12.70%. We have tried to eliminate this minor secondary phase by using various sintering conditions, without success. Similar structural studies of $La_{0.7-x}Lu_xSr_{0.3}MnO_3$ samples show the formation of a secondary phase $LuMnO_3$ [12,13], for which the study by high-resolution transmission electron microscopy (HRTEM) showed the coexistence of orthorhombic and rhombohedral lattice symmetry within the same grain.

3.4. Magnetic properties

Fig. 3 presents the magnetization of $(La_{0.70-x}Y_x)Ba_{0.30}Mn_{1-x}Fe_xO_3$ ($x = 0.0$, 0.10, 0.20 and 0.30) as a function of tempera-

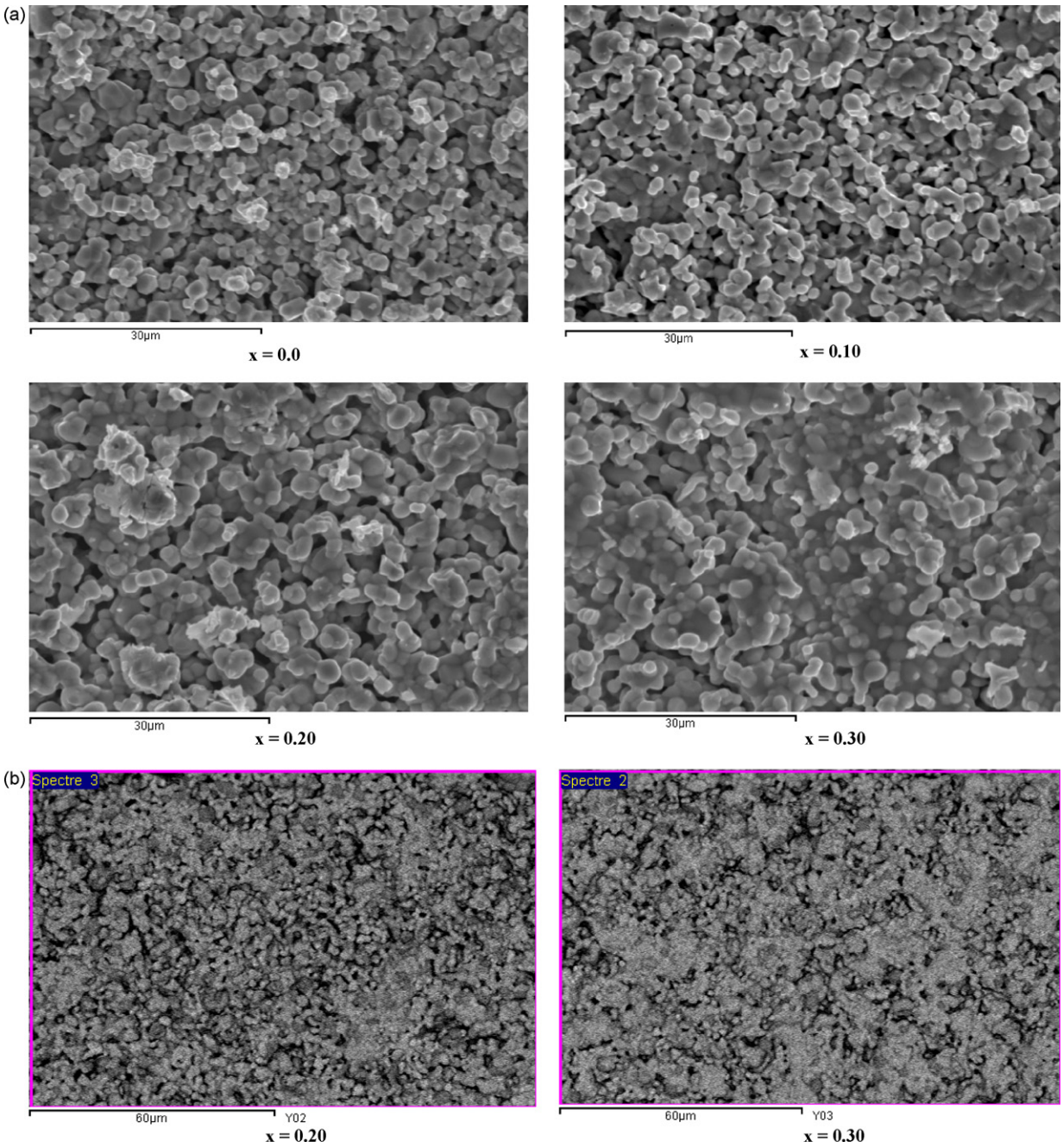

Fig. 1. (a) SEM micrographs of $(La_{0.70-x}Y_x)Ba_{0.30}Mn_{1-x}Fe_xO_3$ samples. (b) SEM micrographs of the samples with $x = 0.20$ and 0.30 (BSE scanning mode).

ture in a 0.01 T magnetic field in both the zero-field-cooled (ZFC) and field-cooled (FC) processes. With decreasing temperature, the samples with $x = 0.0$ and 0.10 exhibit a magnetic transition from a paramagnetic (PM) to a ferromagnetic (FM) state. The Curie temperature, T_C, is 342 and 121 K for $x = 0.0$ and 0.10, respectively (here T_C is defined as the intersection of the steepest slope of $M(T)$ with the temperature axis, as indicated in the figure). The remarkable decrease of transition temperature T_C in presence of 10% of Y and 10% of Fe is due to the reduction of the rate of Mn^{3+} ions and the increase of the rate of Fe^{3+}. This encourages the super-exchange interaction (Fe^{3+}–O–Mn^{4+}, Fe^{3+}–O–Mn^{3+} and Fe^{3+}–O–Fe^{3+}) against the double-exchange interaction (Mn^{3+}–O–Mn^{4+}). The decrease of T_C can also be explained by the insertion of Y^{3+} ions having a small ionic radius compared to La^{3+} ions as observed in $La_{0.7-x}Y_xCa_{0.3}MnO_3$ [14].

The inset curve of Fig. 3 shows two temperatures (θ_f and θ_P) for the sample with $x = 0.10$. The temperature θ_f is called the ferromagnetic Curie temperature and θ_P is the paramagnetic Curie temperature. Well above the Curie temperature, such material behaves like a paramagnetic material and has well defined susceptibility given by the Curie–Weiss law, $\chi = C/(T - \theta_P)$, where C is the Curie constant. The inverse of the susceptibility $(\chi)^{-1}$ is plotted for the $x = 0.10$ sample against temperature. The value of θ_f has been considered as that temperature for which $(\chi)^{-1}$ becomes zero. The value of $\theta_f = 117$ K so obtained is almost comparable with the value $T_C = 121$ K. At and below this temperature the sample becomes ferromagnetic. The paramagnetic Curie temperature θ_P is determined from the curve by extrapolating the straight line portion of the curve toward the temperature axis, as shown in the inset curve of Fig. 3 for the sample with $x = 0.10$. The difference observed

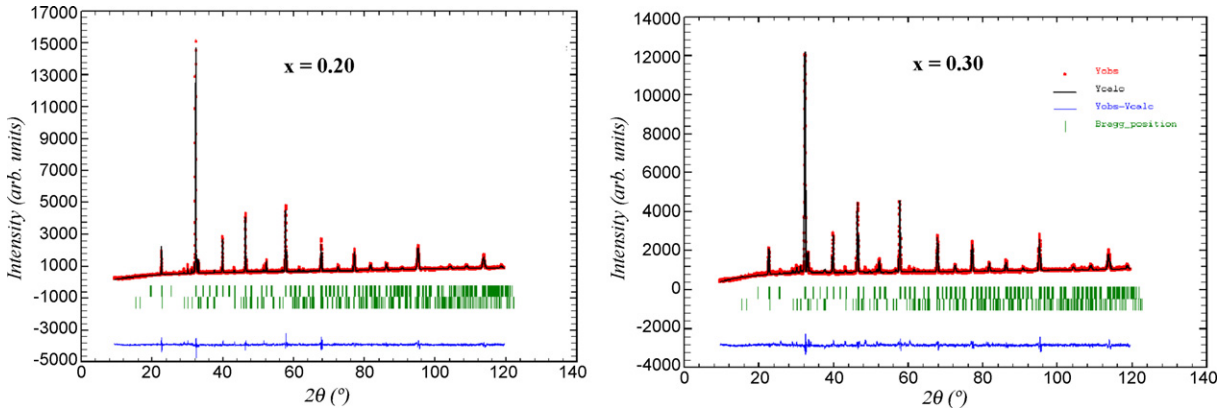

Fig. 2. Measured (open symbols) and calculated (solid lines) X-ray diffraction patterns for $x = 0.20$ and 0.30. Positions for the Bragg reflections are marked by vertical bars. Differences between the observed and the calculated intensities are shown at the bottom of the figure. Second set of vertical bars refers to the $YMnO_3$ minority phase.

between $T_C = 121$ K and $\theta_P = 227$ K for the sample with $x = 0.10$ indicates a presence of magnetic inhomogeneities in the paramagnetic phase.

Apparently, with increasing Y and Fe content the magnetic transition is broadened. From Fig. 3 we can see that the M–(T) curves for samples with $x = 0.20$ and 0.30 are not typical of a "classical" ferromagnet. This widening can be assigned to a magnetic disorder due to the presence of the minority phase of $YMnO_3$ already identified by X-ray diffraction. Such chemical inhomogeneities and the numerous grain boundaries resulting from the small-sized grains (Table 2) may be the reason of the widening of the magnetic transition, as it has been observed in other granular manganites [15,16]. Indeed, previous works show that the width of the magnetic transition decreases with the increase of the grain size in the sample [17,18].

A previous work of Tlili et al. [19] shows a decrease in the Curie temperature (T_C) from 335 to 225 K when the rate of Fe increases from $x = 0$ to 0.10 in $La_{0.70}Ca_{0.15}Sr_{0.15}Mn_{1-x}Fe_xO_3$ sample. Several authors have already reported the effect of Fe doping [20–23]. In all cases the same trend is observed: as the Fe doping level in the sample increases, the transition temperature (T_C) and the magnetization systematically decrease. It was also reported that replacing La by small amount of Y in polycrystalline $La_{0.67}Ca_{0.33}MnO_3$ results in a decrease of T_C [24]. The decrease of T_C is mainly attributed to a decrease of the Mn–O–Mn bond angle due to decrease of the mean ionic radius $\langle r_A \rangle$ of the A-site cation. This is consistent with

Table 3
Crystallographic data for $(La_{0.70-x}Y_x)Ba_{0.30}Mn_{1-x}Fe_xO_3$ perovskites from X-ray diffraction measurements at room temperature.

Sample	0.0	0.10	0.20	0.30
Space group	$R\bar{3}c$	*Pbnm*	*Pbnm*	*Pbnm*
a (Å)	5.5336 (2)	5.5199 (2)	5.5151 (3)	5.5169 (2)
b (Å)	5.5336 (2)	5.5384 (2)	5.5240 (4)	5.5180 (2)
c (Å)	13.4838 (4)	7.8077 (4)	7.8241 (3)	7.8213 (3)
V (Å^3)	357.591 (9)	238.698 (5)	238.369 (6)	238.098 (9)
(La/Ba/Y)				
x	0	0.0038 (15)	−0.0029 (17)	0.0012 (3)
y	0	−0.0003 (1)	−0.0031 (5)	−0.0024 (6)
z	1/4	1/4	1/4	1/4
B	0.33 (4)	0.44 (6)	0.29 (3)	0.25 (3)
(Mn/Fe)				
x	0	1/2	1/2	1/2
y	0	0	0	0
z	0	0	0	0
B	0.08 (7)	0.39 (2)	0.26 (6)	0.47 (3)
(O1)				
x	0.463 (3)	0.5422 (5)	0.4835 (9)	0.4531 (4)
y	0	−0.0325 (2)	0.0045 (1)	0.0418 (9)
z	1/4	1/4	1/4	1/4
(O2)	0.80 (7)	1.02 (9)	1.02 (9)	1.02 (9)
x	–	0.2391 (2)	0.2521 (2)	0.2259 (2)
y	–	0.2568 (7)	0.2701 (3)	0.2377 (6)
z	–	0.5073 (3)	0.5306 (6)	0.4865 (6)
B	–	1.02 (9)	1.02 (9)	1.02 (9)
R_P	4.49	5.02	4.47	3.74
R_{Wp}	6.77	7.83	6.17	5.06
χ^2	5.85	5.16	2.92	2.60
$d_{(Mn/Fe)-O1}$ (Å)	1.964 (13)	1.974 (10)	1.958 (2)	1.986 (14)
$d_{(Mn/Fe)-O2}$ (Å)	–	1.88 (11)	1.90 (6)	1.91 (5)
$\Theta_{(Mn/Fe)-O1-(Mn/Fe)}$ (°)	168.0 (4)	162.80 (4)	174.80 (4)	159.80 (6)
$\Theta_{(Mn/Fe)-O2-(Mn/Fe)}$ (°)	–	177.00 (5)	165.00 (2)	170.00 (2)
$La_{0.7-x}Y_xBa_{0.3}Mn_{1-x}Fe_xO_3$ weight fractions (in %)	100%	100%	90.68%	87.30%

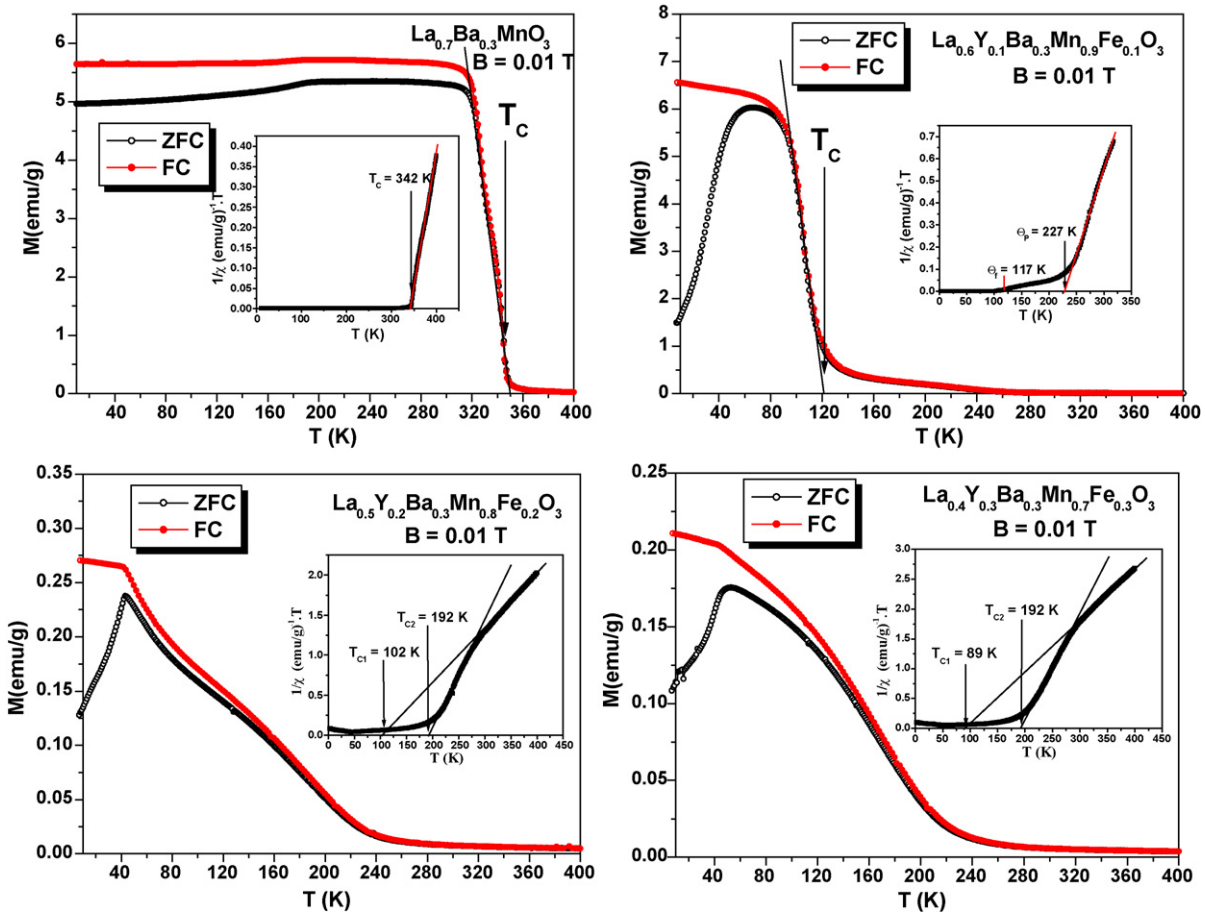

Fig. 3. Temperature dependence of magnetization under ZFC and FC processes in an applied field of 0.01 T for $(La_{0.70-x}Y_x)Ba_{0.30}Mn_{1-x}Fe_xO_3$. The insets show the $1/\chi$ curves.

the decrease of the carrier bandwidth (W) of the e_g band resulting from an overlap between 3d orbitals of the metallic ions and 2p orbitals of the oxygen ions [25].

In addition to the mentioned decrease of T_C with increasing Fe concentration, the transition width also increases quite appreciably with increasing Fe concentration, suggesting suppression of the double-exchange mechanism. This is due to the fact that Fe^{3+} substitution for Mn^{3+} reduces the number of available hopping sites for the Mn $e_g(\uparrow)$ electron and suppresses the double-exchange, resulting in the reduction of ferromagnetism [19–23].

In order to understand this intermediate region, we represent the variation of the inverse of the susceptibility versus temperature for the samples with $x = 0.20$ and 0.30 (inset of Fig. 3). These curves show the presence of two transition temperatures noted T_{C1} and T_{C2}. The magnetic studies of Kolat et al. [26] showed two maxima T_{C1} and T_{C2} in the (dM/dT)–T curve of $La_{0.67}Ca_{0.33}Mn_{0.9}V_{0.1}O_3$ which could be interpreted as the presence of two different phases identified by SEM photographs: one has a composition of $La_{0.73}Ca_{0.27}Mn_{0.96}V_{0.04}O_3$ and the other has a composition of $La_{0.4}Ca_{0.6}Mn_{0.21}V_{0.79}O_3$. The same observation exists for $La_{0.67}Ca_{0.33}Mn_{0.7}B_{0.3}O_3$ sample [27]. In the case of $SrRu_{0.8}Cu_{0.2}O_3$ sample the authors show three features at 155, 65 and 32 K [28]. The features at 155 K indicate ferromagnetic ordering due to the $SrRuO_3$ impurity phase. Whereas, the feature at 65 K is due to ferromagnetic transition of copper substituted phase ($SrRu_{0.8}Cu_{0.2}O_3$). In our case, we notice that both samples, $x = 0.20$ and 0.30, present the same temperature $T_{C2} = 192$ K. It brings us to propose two hypotheses about the origin of the temperature T_{C2}:

(i) It can be due to the presence of the minority phase $YMnO_3$.
(ii) It can be due to the chemical inhomogeneity of grains forming the sample.

To verify these two hypotheses, further investigations are needed. A study by transmission electronic microscopy (TEM) seems necessary to verify the structure within a unique grain. This study will be coupled with a semi-quantitative energy dispersive X-ray analysis (EDX) on grains presenting different contrasts in order to verify their chemical composition.

For the undoped sample the magnetization (M_{FC}) remains constant up to about 320 K and then decreases at higher temperatures. For all doped samples ($x \geq 0.10$) the field-cooled magnetization (M_{FC}) is found to decrease continuously with increasing temperature, while the zero-field-cooled magnetizations (M_{ZFC}) increase significantly with increasing temperature up to a maximum value, and then decrease. One may conclude that doped samples have an important antiferromagnetic contribution. Thus, for all Fe-doped samples there could be a competing antiferromagnetic component due to the increase of the number of units Fe^{3+}–O–Mn^{4+}, Fe^{3+}–O–Mn^{3+} and Fe^{3+}–O–Fe^{3+}.

Table 4
Results of refinement of the secondary phase $YMnO_3$.

Phase 2: $YMnO_3$ space group: $P6_3cm$ (hexagonal)		
Sample	$x = 0.20$	$x = 0.30$
a (Å)	6.1353 (12)	6.1287 (14)
c (Å)	11.4360 (4)	11.4631 (4)
V (Å^3)	372.799 (10)	372.885 (7)
Weight fractions (in %)	9.32	12.70

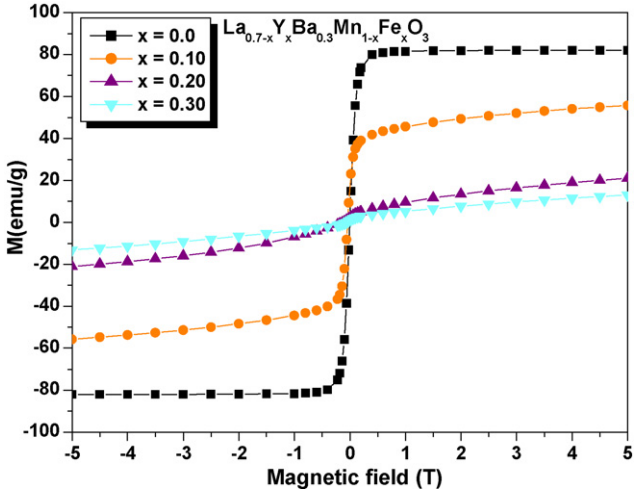

Fig. 4. Magnetization as function of applied field at 2 K (a zoomed region is shown in Fig. 6).

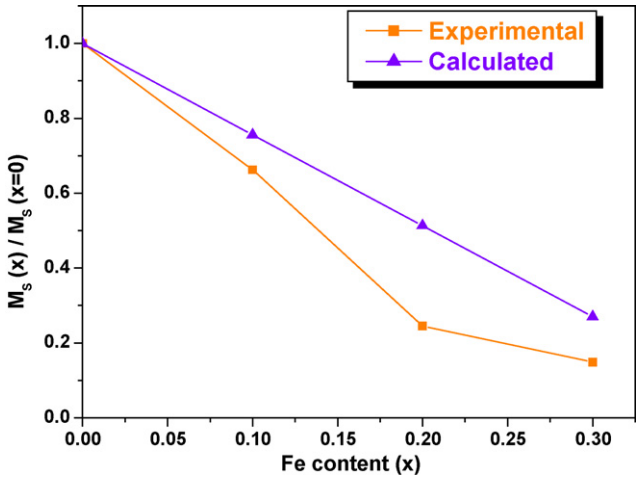

Fig. 5. Ratio of saturation moments [M_S (x)/M_S (x = 0)] versus Fe content (x).

For $x \geq 0.10$, the ZFC and FC curves display irreversibility (Fig. 3) which indicates the distortion of a long-range ferromagnetic order [29]. The ZFC magnetization exhibits a cusp that appears at around 68, 44, 46 K respectively for $x = 0.10$, 0.20 and 0.30. Such a behavior is typical of spin-glasses which must have arisen due to the frustration caused by the competition between ferromagnetic (double-exchange) and antiferromagnetic (super-exchange) interactions [30–32]. A similar behavior has been reported by Cao et al. [33] and attributed to the spin-glass behavior. The work of Gutierrez et al. [34] shows the presence of a spin-glass behavior in $La_{0.7}Pb_{0.3}Mn_{1-x}Fe_xO_3$ sample (for $x = 0.20$; $T_{SG} = 55$ K and for $x = 0.30$; $T_{SG} = 45$ K). In the same way, a system of spin-glass is present in $La_{0.7}Sr_{0.3}Mn_{1-x}Ti_xO_3$ ($x = 0.30$; $T_{SG} = 33$ K) [35].

To better understand the effect of the substitution of the manganese ion by iron, we report in Fig. 4 the magnetization variation with field at $T = 2$ K. The magnetization isotherms show a decrease of saturation magnetization when increasing the iron content. The magnetization becomes saturated in a field of 0.6 T for the undoped sample. For the doped samples the saturation is attained at a greater field.

While considering only the magnetic moment of the Mn^{3+} and Mn^{4+} ions, the calculated values of the saturation magnetic moment are given by:

$$M_{Sat}(cal) = 2 \times \left[\frac{4}{2} \times n_{Mn^{3+}} + \frac{3}{2} \times n_{Mn^{4+}}\right]$$

The obtained calculated values are very far from experimental values obtained from M–H curves (Fig. 4). The M_{Sat}(cal) values are $3.3\mu_B$; $2.9\mu_B$ and $2.5\mu_B$, while the M_{Sat}(exp) values are $2.35\mu_B$; $0.87\mu_B$and $0.53\mu_B$, respectively, for $x = 0.10$, 0.20 and 0.30. This means that it is not enough to consider only the contribution of the magnetic moment of the Mn^{3+} and Mn^{4+} ions. The Fe^{3+} ([Ar] $3d^5$) ion possesses an incomplete 3d layer and carries a magnetic moment. The Fe ions in the doped samples do not add up to the total moment since the variation of $M(H)$ at $T = 2$ K does not show any additional contribution to the saturation magnetization (Fig. 4).

We can then explain the saturation of the magnetic moment on the basis of a single-ion model with antiferromagnetic arrangements of the Mn and Fe spins. The substitution of Mn^{3+} by Fe^{3+} ions triggers antiferromagnetic interactions between the Fe^{3+} ions and Mn^{4+} ions. On the basis of an antiferromagnetic arrangement

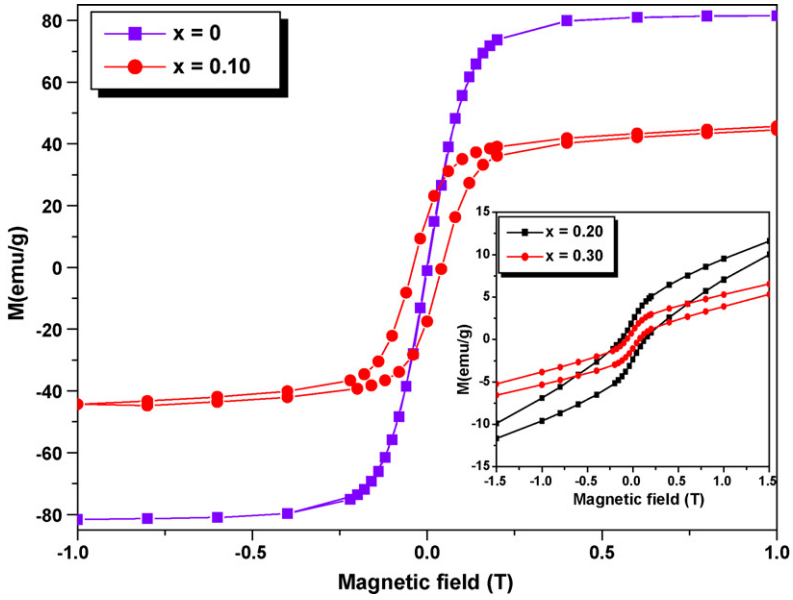

Fig. 6. Hysteresis loops at 2 K and low fields, for $La_{0.7-x}Y_xBa_{0.3}Mn_{1-x}Fe_xO_3$. Main panel, $x = 0$ and 0.10; inset, $x = 0.20$ and 0.30.

model of the Mn and Fe ions, the calculated values of the saturation magnetic moment per formula unit M_{Sat} (cal) can be expressed as:

$$M_{Sat}(cal) = (M_{SatMn^{3+}})(n_{Mn^{3+}}) + (M_{SatMn^{4+}})(n_{Mn^{4+}}) - (M_{SatFe^{3+}})(n_{Fe^{3+}})$$

where $M_{SatMn^{3+}}$ (=4μ_B), $M_{SatMn^{4+}}$ (=3μ_B), $M_{SatFe^{3+}}$ (=5μ_B) are the magnetic moments (neglecting the orbital contribution) and $n_{Mn^{3+}}$, $n_{Mn^{4+}}$, $n_{Fe^{3+}}$ are respectively the contents of the Mn^{3+}, Mn^{4+}, Fe^{3+} ions. In Fig. 5 we plot the ratio of M_S (x)/M_S (x = 0) versus Fe content. The experimental data are close to the calculated values, which confirm the antiferromagnetic arrangement between the Fe and Mn ions. Early studies of Ahn et al. [21] showed that the Fe doping in the $La_{1-x}Ca_xMnO_3$ sample suppressed ferromagnetism and lead to a canted spin antiferromagnetic phase with 0.09 at.% Fe-ion. They suggested that Fe ions do not take part in double-exchange mechanism but they encourage super-exchange antiferromagnetism.

A typical plot of magnetization as a function of magnetic field (M–H loop) measured at 2 K, at low fields, is shown in Fig. 6 for all samples. A ferromagnetic-like $M(H)$ loop with a very weak coercive field H_{coerc}, was observed for the sample with x = 0.0. This ferromagnetic behavior is characterized by a quick saturation at ∼0.4 T and a saturation moment of ∼80 emu/g. For the doped samples (x = 0.10, 0.20 and 0.30), the magnetization loops are essentially different from the one of the undoped sample. Fig. 6 clearly shows the existence of a large ferromagnetic component, as evidenced by the noticeable hysteresis at low fields. In addition, the magnetization does not saturate at 5 T (Fig. 4) and, in the case of the spin-glass compound it increases almost linearly with field at high fields.

The behavior of the spin-glass type is generally due to the existence of ferromagnetic and antiferromagnetic interactions. It can also be due simply to a random antiferromagnetic distribution. However, at low temperature, such behavior makes impossible the existence of a long-range magnetic order. The competition between ferromagnetic and antiferromagnetic interactions results in a spin-glass behavior. A spin-glass system corresponds to the presence of ferromagnetic nano-domains coupled by complex interactions (ferromagnetic and antiferromagnetic interactions). The competition between the ferromagnetic double-exchange interaction and the antiferromagnetic super-exchange interaction produces spin frustration and is responsible for the occurrence of spin-glass.

4. Conclusion

In summary, we have studied the structure and magnetic properties of $La_{0.7-x}Y_x$ $Ba_{0.3}Mn_{1-x}Fe_xO_3$ for $0 \le x \le 0.3$. The structural study by X-ray diffraction revealed a structural transition from rhombohedral to orthorhombic symmetry when $x \ge 0.10$. A minor secondary $YMnO_3$ phase is present in samples with x = 0.20 and 0.30. The magnetic characterizations showed that the substitution of the manganese by iron considerably weakens magnetism. The existence of a competition between the ferromagnetic interaction Mn^{4+}–O–Mn^{3+} and antiferromagnetic interactions Fe^{3+}–O–Fe^{3+}, Fe^{3+}–O–Mn^{4+} and Fe^{3+}–O–Mn^{3+} lead the Fe-doped sample to behave like a spin-glass system.

Acknowledgment

Authors acknowledge the Tunisia-France exchange program DGRS-CNRS project n° 09//R 11-52.

References

[1] S. Jin, T.H. Tiefel, M. McCormack, R.A. Fastnacht, R. Ramesh, L.H. Chen, Science 264 (1994) 413.
[2] P. Schiffer, A.P. Ramirez, W. Bao, S.-W. Cheong, Phys. Rev. Lett. 75 (1995) 3336.
[3] G.H. Jonker, J.H. Van Santen, Physica 16 (1950) 337.
[4] I.O. Troyanchuk, M.V. Bushynski, N.V. Pushkarev, H. Szymczak, K. Barner, J. Magn. Magn. Mater. 225 (2001) 331.
[5] H.M. Rietveld, J. Appl. Crystallogr. 2 (1969) 65.
[6] Z.Q. Li, E.Y. Jiang, S.W. Ren, D.L. Hou, P. Wu, H.L. Bai, Phys. Status Solidi A 195 (2) (2003) 429–433.
[7] P.G. Radaelli, M. Marezio, H.Y. Hwang, S.-W. Cheong, J. Solid State Chem. 122 (1996) 444–447.
[8] R. Vengadesh Kumara Mangalam, A. Sundaresan, J. Chem. Sci. 118 (2006) 99–103.
[9] H.L. Yakel, W.C. Koehler, E.F. Bertant, E.F. Forrat, Acta Crystallogr. 16 (1963) 957.
[10] G.A. Smolenskii, V.A. Bokov, J. Appl. Phys. 35 (1964) 915.
[11] G.H. Rao, J.R. Sun, A. Kattwinkel, L. Haupt, K. Bärner, E. Schmitt, E. Gmelin, Physica B 269 (1999) 379.
[12] B.Z. Sun, L.L. He, F. Luo, C.H. Yan, Mater. Chem. Phys. 98 (2006) 415.
[13] B.Z. Sun, L.L. He, F. Luo, C.H. Yan, Physica B 367 (2005) 249.
[14] R.S. Freitas, L. Ghivelder, F. Damay, F. Dias, L.F. Cohen, Phys. Rev. B 64 (2001) 144404.
[15] C. Vazquez, M.C. Blanco, M.A. Lopez-Quintela, R.D. Sanchez, J. Rivas, S.B. Oseroff, J. Mater. Chem. 8 (1998) 991.
[16] N. Zhang, W.P. Ding, W. Zhong, D.Y. Xing, Y.W. Du, Phys. Rev. B 56 (1997) 8138.
[17] R.D. Sanchez, J. Rivas, C. Vazquez-Vazquez, A. Lopez-Quintela, M.T. Causa, M. Tovar, S. Oseroff, Appl. Phys. Lett. 68 (1) (1996) 134–136.
[18] C. Krishnamoorthy, K. Sethupathi, V. Sankaranarayanan, R. Nirmala, S.K. Malik, J. Alloys Compd. 438 (2007) 1–7.
[19] M.T. Tlili, M. Bejar, E. Dhahri, M. Sajieddine, E.K. Hlil, J. Magn. Magn. Mater. (2010), doi:10.1016/j.jmmm.2009.12.040.
[20] Q. Huang, Z.W. Li, C.K. Ong, J. Phys.: Condens. Matter 13 (2001) 4033.
[21] K.H. Ahn, X.W. Wu, K. Liu, C.L. Chien, J. Appl. Phys. 81 (8) (1997) 5505.
[22] V. Dayal, S. Keshri, Solid State Commun. 142 (2007) 63.
[23] M. Nadeem, M.J. Akhtar, A.Y. Khan, Solid State Commun. 134 (2005) 431.
[24] S. Jin, H.M. OBryan, T.H. Tiefel, Appl. Phys. Lett. 66 (1995) 382.
[25] K. Bajaj, V. Bagwe, J. Jesudasan, P. Raychaudhuri, Solid State Commun. 138 (2006) 549–552.
[26] V.S. Kolat, H. Gencer, S. Atalay, Physica B 371 (2006) 199–204.
[27] V.S. Kolat, H. Gencer, M. Gunes, S. Atalay, Mater. Sci. Eng. B 140 (2007) 212–217.
[28] R.V.K. Mangalam, A. Sundaresan, Mater. Res. Bull. 44 (2009) 576–580.
[29] S.L. Young, H.Z. Chen, L. Horng, J.B. Shi, Y.C. Chen, Jpn. J. Appl. Phys. 40 (2001) 4878.
[30] J.J. Blanco, M. Insausti, I. Gil de Muro, L. Lezama, T. Rojo, J. Solid State Chem. 179 (2006) 623.
[31] J. Takeuchi, S. Hirahara, T.P. Dhakal, K. Miyoshi, K. Fujiwara, J. Magn. Magn. Mater. 226 (2001) 884.
[32] R. Laiho, K.G. Lisunov, E. Lähderanta, J. Salminen, V.S. Zakhvalinskii, J. Magn. Magn. Mater. 250 (2002) 267.
[33] G. Cao, J. Zhang, S. Wang, J. Yu, Y. Xu, S. Cao, C. Jing, X. Shen, J. Magn. Magn. Mater. 310 (2007) 777.
[34] J. Gutierrez, A. Pena, J.M. Barandiaran, J.L. Pizarro, T. Hemandez, L. Lezama, M. Insausti, T. Rojo, Phys. Rev. B 61 (2000) 9028.
[35] N. Kallel, M. Oumezzine, H. Vincent, J. Magn. Magn. Mater. 320 (2008) 1810–1816.